

Article pubs.acs.org/JACS

Asymmetric Design of Spin-Crossover Complexes to Increase the **Volatility for Surface Deposition**

Miguel Gakiya-Teruya, Xuanyuan Jiang, Duy Le, Ökten Üngör, Abdullah J. Durrani, John J. Koptur-Palenchar, Jun Jiang, Tao Jiang, Mark W. Meisel, Hai-Ping Cheng, Xiao-Guang Zhang, Xiao-Xiao Zhang, Talat S. Rahman, Arthur F. Hebard, and Michael Shatruk*



Cite This: J. Am. Chem. Soc. 2021, 143, 14563-14572



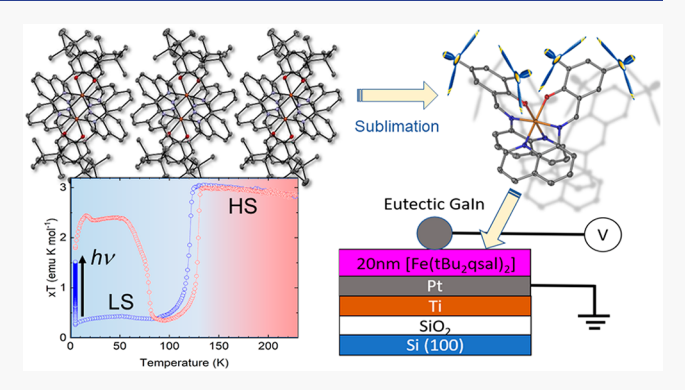
ACCESS

Metrics & More

Article Recommendations

s Supporting Information

ABSTRACT: A mononuclear complex $[Fe(tBu_2gsal)_2]$ has been obtained by a reaction between an Fe(II) precursor salt and a tridentate ligand 2,4-di(tert-butyl)-6-((quinoline-8-ylimino)methyl)phenol (tBu₂qsalH) in the presence of triethylamine. The complex exhibits a hysteretic spin transition at 117 K upon cooling and 129 K upon warming, as well as light-induced excited spinstate trapping at lower temperatures. Although the strongly cooperative spin transition suggests substantial intermolecular interactions, the complex is readily sublimable, as evidenced by the growth of its single crystals by sublimation at 573 → 373 K and $\sim 10^{-3}$ mbar. This seemingly antagonistic behavior is explained by the asymmetric coordination environment, in which the tBu substituents and quinoline moieties appear on opposite sides of the



complex. As a result, the structure is partitioned in well-defined layers separated by van der Waals interactions between the tBu groups, while the efficient cooperative interactions within the layer are provided by the quinoline-based moieties. The abrupt spin transition is preserved in a 20 nm thin film prepared by sublimation, as evidenced by abrupt and hysteretic changes in the dielectric properties in the temperature range comparable to the one around which the spin transition is observed for the bulk material. The changes in the dielectric response are in excellent agreement with differences in the dielectric tensor of the low-spin and high-spin crystal structures evaluated by density functional theory calculations. The substantially higher volatility of $[Fe(tBu_2qsal)_2]$, as compared to a similar complex without tBu substituents, suggests that asymmetric molecular shapes offer an efficient design strategy to achieve sublimable complexes with strongly cooperative spin transitions.

INTRODUCTION

Spin crossover (SCO) is one of the most extensively investigated examples of magnetic, structural, and optical bistability in molecule-based materials. The fundamentals of SCO behavior have been studied since the 1960s. Over the past decade, these studies have focused on a deeper understanding of the SCO phenomenon, in particular with regard to the ferroelastic nature of the spin transition,^{2,3} the excited state relaxation cascades during light-induced spin-state switching, 4-7 and the ability of advanced theoretical models to predict more reliably the occurrence of SCO and its parameters.8-11

Along with the deeper insight into the fundamental nature of SCO, broad recent efforts have emerged aimed to incorporate SCO complexes in hybrid materials and devices. These works aim to leverage the large differences in the magnetic, structural, and optical properties of the low-spin (LS) and high-spin (HS) electronic configurations to induce substantial changes in the response of a system to external stimuli, such as electric currents, 12,13 electric or magnetic polarization, 14 and optical

excitations. 15,16 Driven by the interest in practical applications of such materials, several research teams have been actively exploring the use of SCO complexes as thin films, monolayers, or even single molecules incorporated in electronic devices. Among noteworthy recent achievements is the modulation of carrier mobility in graphene by SCO nanoparticles deposited on this ubiquitous two-dimensional (2D) material, 17 the study of the dynamics of light-induced SCO in a molecular layer deposited on the Au(111) surface, 16 the demonstration of a spin-filtering response from a single SCO molecule, 18 and high-resolution surface temperature matching with an SCO film.19

Received: May 3, 2021 Published: September 2, 2021





All these efforts notwithstanding, the preparation of ultrathin interface heterostructures based on SCO complexes remains a nascent and challenging research area. The central issue in these studies is the preservation of the spin-state switching behavior when the bulk material is deposited on a substrate. Under such conditions, the molecule might not only lose its SCO properties but even decompose due to the molecule—substrate interaction or the high temperature—high vacuum conditions used for the film deposition. An alternative approach is to deposit the SCO molecules on substrates directly from solutions, but such method introduces the complications related to the possible coabsorption of solvent molecules or counterions that might compete for surface coverage with the SCO moieties and lead to poorly reproducible behavior.

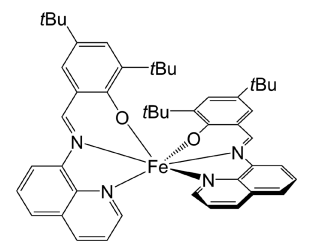
In other words, the preparation of thin films of functional magnetic molecules by clean, facile sublimation protocols remains a widespread and significant challenge. To date, only a handful of SCO complexes have been sublimed onto inorganic substrates. The majority of them required high-vacuum conditions ($<10^{-6}$ mbar) to transport the molecules through the vapor phase to the substrate. To the best of our knowledge, only complexes of the type $[Fe(Bpz_2)_2(L_2)]$, where $L_2 = 2,2'$ -bipyridine or 1,10-phenanthroline, have been successfully sublimed onto substrates under relatively low vacuum ($\sim 10^{-2}$ mbar). Consequently, they represent the most studied SCO compounds as relevant to the investigation of thin films and interfaces.

The ease of sublimation of SCO complexes can be improved by introduction of substituents known to increase the volatility of other molecules. In particular, it is well established that tertbutyl (tBu) groups allow higher volatility of organic and inorganic molecules, as shown by the use of mono-, di-, and multinuclear metal complexes with such substituents for the preparation of oxide and intermetallic materials by metalorganic chemical vapor deposition (MO-CVD) followed by high-temperature decomposition of such molecular precursors. 25-27 The introduction of such substituents unavoidably decreases the intermolecular forces in the solid state, thus lowering the sublimation enthalpy. Such an effect, however, can be detrimental to the SCO behavior, as strong intermolecular interactions in the solid state are crucial to achieving abrupt and hysteretic spin transitions that make SCO materials so appealing for practical applications.

We hypothesized that this dilemma could be resolved by creating SCO complexes with an asymmetric arrangement of the coordination sphere. Positioning the tBu substituents on one side of the complex while leaving the other side open for efficient intermolecular interactions, such as $\pi-\pi$ and $\sigma-\pi$ contacts, should help compartmentalize the structure into the regions with weaker and stronger intermolecular contacts. Such compartmentalization can help increase the volatility while preserving the strong elastic coupling between the neighboring molecules, which is crucial for maintaining the cooperative SCO behavior with the abrupt spin transition.

Herein, we apply such a strategy to a homoleptic SCO complex based on the combination of an Fe^{II} ion with tridentate Schiff-base type ligands. The ligands of Schiff-base type are well established to provide an appropriate ligand field strength for the occurrence of SCO in Fe^{II} complexes. $^{28-35}$ We demonstrate that the complex $[Fe(tBu_2qsal)_2]$ (Scheme 1), where tBu_2qsal^- is a deprotonated form of 2,4-di(tert-butyl)-6-((quinoline-8-ylimino)methyl)phenol (tBu_2qsalH), undergoes

Scheme 1. Molecular Structure of $[Fe(tBu_2qsal)_2]$



an abrupt spin transition centered at 123 K with a 12 K thermal hysteresis. The complex also exhibits light-induced spin-state switching at low temperatures. Theoretical modeling confirms that the presence of the $t\mathrm{Bu}$ substituents leads to reduced intermolecular interactions along the lattice planes separated by these groups. The complex can be easily sublimed at 573 K and $\sim 10^{-3}$ Torr, or even at lower temperatures if the vacuum is higher, allowing the deposition of thin films that preserve the SCO behavior similar to that observed in the bulk sample.

RESULTS AND DISCUSSION

Synthesis and Thermal Stability. The neutral mononuclear complex $[Fe(tBu_2qsal)_2]$ was crystallized by layering a solution of $[Fe(H_2O)_6](CIO_4)_2$ in acetonitrile with a solution of tBu_2qsalH and Et_3N in acetone. The plate-shaped darkgreen crystals of $[Fe(tBu_2qsal)_2]$ show good stability in air. Thermogravimetric analysis revealed that the complex was stable up to $\sim\!600$ K (Figure S1), while an abrupt step above 420 K indicates that the complex might be partially sublimable in a flow of argon gas. As a result, it was possible to achieve the crystal growth of this material by vapor transport in a temperature gradient of 553 K \rightarrow 373 K at a relatively low vacuum of $\sim\!10^{-3}$ mbar. A representative crystal grown by such method is shown in the inset of Figure 1.

Crystal Structure. The crystal structure of $[Fe(tBu_2qsal)_2]$ was determined by single-crystal X-ray diffraction (XRD) performed at 100 and 230 K (Table S1). The complex crystallizes as a solvent-free material in the monoclinic space

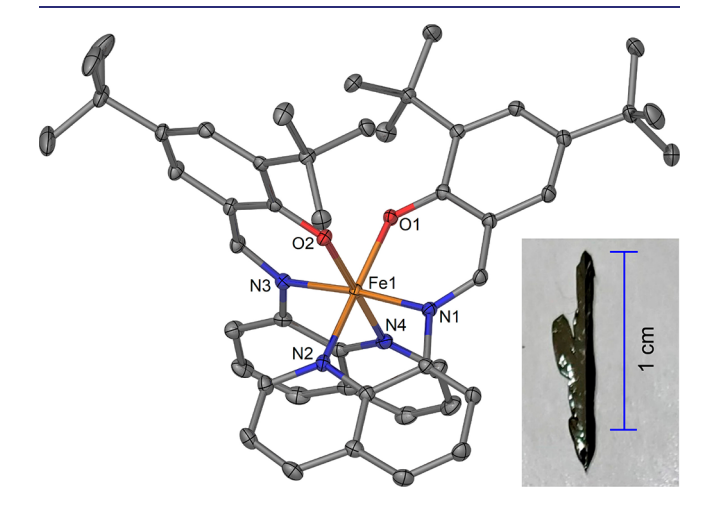


Figure 1. Crystal structure of $[Fe(tBu_2qsal)_2]$, with the thermal ellipsoids at the 50% probability level. Only the first coordination sphere of the Fe^{II} ion is labeled. The H atoms are omitted for clarity. Inset: a representative crystal grown by thermal-gradient vapor transport.

group $P2_1/c$. The structure of the molecule clearly shows the juxtaposed regions dominated by the tBu substituents or by the quinoline moieties (Figure 1). We note that analogous complexes have been reported for the Co^{II} and Ni^{II} ions, although they do not exhibit SCO. 36,37

The Fe^{II} ion resides in an N_4O_2 coordination environment created by two *mer*-coordinating tridentate tBu_2qsal^- ligands. The average Fe-N bond length elongates from 1.949(2) Å at 100 K to 2.167(2) Å at 230 K. The elongation of the average Fe-O bond length is smaller but also substantial, from 1.945(1) at 100 K to 1.997(1) Å at 230 K. These changes clearly indicate that a conversion from the LS to HS structure takes place as the temperature is increased. Moreover, these values agree well with those obtained from density functional theory (DFT) calculations (Table S1) which show that the average Fe-N bond lengths in the LS and HS states are 1.946 and 2.163 Å, respectively, and the average Fe-O bond lengths are 1.958 and 2.001 Å, respectively.

The temperature-induced SCO is also evidenced by the large change in the angular distortion parameter (Σ_{90}), defined as the sum of absolute deviations of the 12 *cis*-X–Fe–X angles (X = N/O) from the ideal octahedral value of 90° (Table 1

Table 1. Bond Lengths and the Σ_{90} Angular Distortion Parameter in the Crystal Structure of $[Fe(tBu_2qsal)_2]$ as a Function of Temperature

	100 K	230 K
	bond lengths, Å	
Fe(1) - O(1)	1.943(1)	2.0107(9)
Fe(1)-O(2)	1.946(1)	1.9839(9)
Fe(1)-N(1)	1.934(1)	2.129(1)
Fe(1)-N(2)	1.959(1)	2.224(1)
Fe(1)-N(3)	1.930(1)	2.181(1)
Fe(1)-N(4)	1.971(1)	2.133(1)
bong angles, deg		
O(1)-Fe(1)-O(2)	86.01(4)	93.51(4)
N(1)-Fe(1)-N(2)	83.33(5)	75.80(4)
N(3)-Fe(1)-N(4)	83.19(5)	76.45(4)
O(i)-Fe(1)-N(j) ^{a}	90.06(5)-93.43(5)	85.98(4)-105.35(4)
$N(k)$ -Fe(1)- $N(l)^b$	91.68(5)-93.53(5)	86.80(4)-94.37(4)
Σ_{90} (cis-N/O-Fe-N/O)	35.6(2)	80.2(1)
$a_i = 1 \text{ or } 2, j = 1, 2, 3, \text{ or } 4.$ $b(k,l) \neq (1,2) \text{ or } (3,4).$		

and Table S1). The distortion parameter is expected to increase dramatically upon conversion from the LS to HS state, 38 as indeed observed experimentally. These changes in the octahedral distortion can be traced back to the substantial change in the chelating angles, N(1)-Fe(1)-N(2) and N(3)-Fe(1)-N(4), which decrease by $\sim 7^{\circ}-8^{\circ}$ each when the LS complex is converted to the HS complex, due to the elongation of the Fe-N distances (Table 1). This decrease is compensated by an increase in the O(1)-Fe(1)-O(2) angle by 7.5° and by the increased spread in the values of the other N-Fe-N and O-Fe-N angles.

The crystal packing shows a distinct 2D structural organization (Figure 2a). The $[Fe(tBu_2qsal)_2]$ molecules pack in layers parallel to (100) lattice planes. Within these layers, the molecules are coupled through $\pi-\pi$ and $\sigma-\pi$ interactions between the quinoline-based sides of the ligands (Figure 2b). In contrast, the phenolic sides, decorated with the tBu substituents, are oriented toward the interlayer space

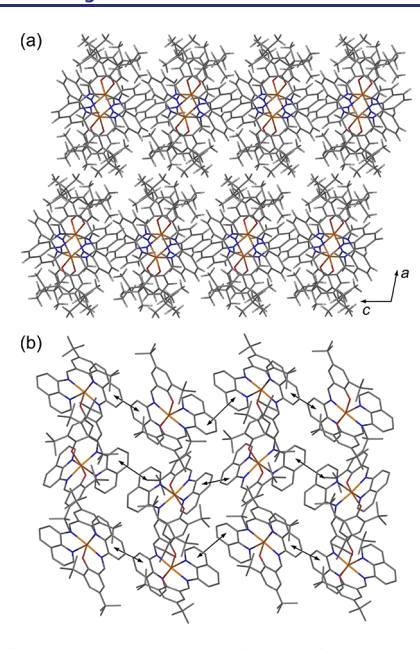


Figure 2. (a) Crystal packing of $[Fe(tBu_2qsal)_2]$ viewed down the *b*-axis to emphasize the layered structure of the material. (b) The $\pi-\pi$ contacts (black arrows) within one layer. Color scheme: Fe = orange, O = red, N = violet, C = gray. The H atoms in (b) are omitted for clarity.

dominated by weak van der Waals interactions between the tBu groups.

Thus, it appears that the layered structural organization of $[Fe(tBu_2qsal)_2]$ is promoted by the introduction of the tBu groups on the periphery of the ligand. Indeed, an examination of the reported crystal structure of a related complex, $[Fe(qnal)_2] \cdot CH_2Cl_2$ (qnal = 1-(((8-quinolinyl)imino)-methyl)-2-naphtholate), which contains a fused benzene ring instead of the tBu substituents (Scheme S1), reveals the lack of any pronounced lower-dimensional structural features: the $[Fe(qnal)_2]$ molecules show efficient intermolecular interactions in all three dimensions (Figure S2).

DFT calculations (see below) revealed that the exfoliation energy, defined as the energy needed to exfoliate a unit area of a single layer of molecules, equals 0.888, 0.927, and 1.236 mJ/m² along the [100], [001], and [010] exfoliation directions, respectively (the views of the structure along [100] and [001] are given in Figure S3 while the view along [010] is given in Figure 2a). These values indicate that the cohesion of the structure is the weakest along the a-axis of the crystal lattice and the strongest along the b-axis. The observed structural organization and calculated exfoliation energies explain the appearance of the crystals of $[Fe(tBu_2qsal)_2]$ as elongated plates, with the largest face corresponding to the (100) lattice plane and the longest direction coinciding with the b-axis of the lattice.

Powder XRD performed on a bulk sample of [Fe($tBu_2qsal)_2$] (Figure S4) revealed that the unit cell parameters (Figure 3a) and volume (Figure 3b) change anomalously and hysteretically. The substantial change in the unit cell volume is in agreement with the observed large changes in the bond lengths between the crystal structures determined at 230 and 100 K (Table 1). These results suggest that the material undergoes an abrupt spin transition with a 12 K thermal hysteresis, corresponding to the HS \rightarrow LS conversion at 117 K and to the reverse LS \rightarrow HS conversion at 129 K.

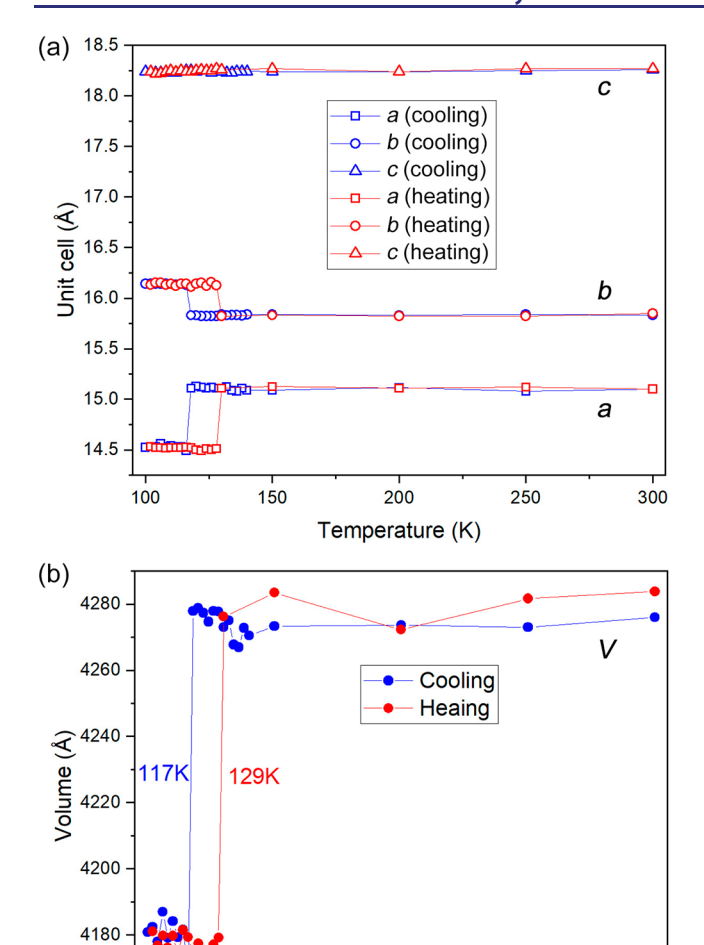


Figure 3. Temperature dependence of the unit cell parameters and volume of $[Fe(tBu_2qsal)_2]$ measured in the cooling (blue symbols) and heating (red symbols) regimes. The lines are guides for the eye. The estimated standard deviations are smaller than the size of the symbols.

200

Temperature (K)

150

250

300

4160

100

Interestingly, although the unit cell exhibits an abrupt collapse along the a-axis at 117 K, it elongates along the b-axis, while the c-axis remains nearly constant in comparison to the other two parameters (Figure 3a). These changes, yet again, agree with the nature of interactions observed in the crystal packing and with the cohesion energies obtained by DFT calculations. While the weak van der Waals interactions between the layers allow for relatively easy compression and expansion of molecules along the a-axis upon the HS \rightarrow LS and LS \rightarrow HS transitions, respectively, the material compensates for these structural changes by a smaller opposite change along the b-axis.

Importantly, we observe that such asymmetric structure of the complex, with the different nature of intermolecular interactions on the opposite sides of the molecule, translates into the distinctly anisotropic structural organization, with the interactions between molecules weakened in the direction perpendicular to certain lattice planes but preserved within the layers parallel to those planes. Such crystal packing allows the preservation of an abrupt spin transition while also rendering the material sublimable under relatively low vacuum conditions $(\sim 10^{-3}$ mbar at 573 K). In contrast, the already mentioned [Fe(qnal)₂] analogue required a much higher vacuum ($\sim 10^{-7}$ mbar at 590 K) for sublimation into a thin-film structure.⁴⁰

Magnetic and Photomagnetic Properties. Magnetic susceptibility (χ) measurements were performed on a crushed polycrystalline sample of $[Fe(tBu_2qsal)_2]$. The χT value of ~ 3.0 emu·mol⁻¹·K observed at room temperature is in agreement with the presence of the HS Fe^{II} ions determined by the crystal structure analysis. As the temperature is decreased, the χT value remains nearly constant, until an abrupt drop in χT takes place at $T_{1/2,\downarrow}=117$ K, indicating the occurrence of a cooperative spin transition to the LS state (the blue curve in Figure 4). Upon heating back to 300 K, a reverse

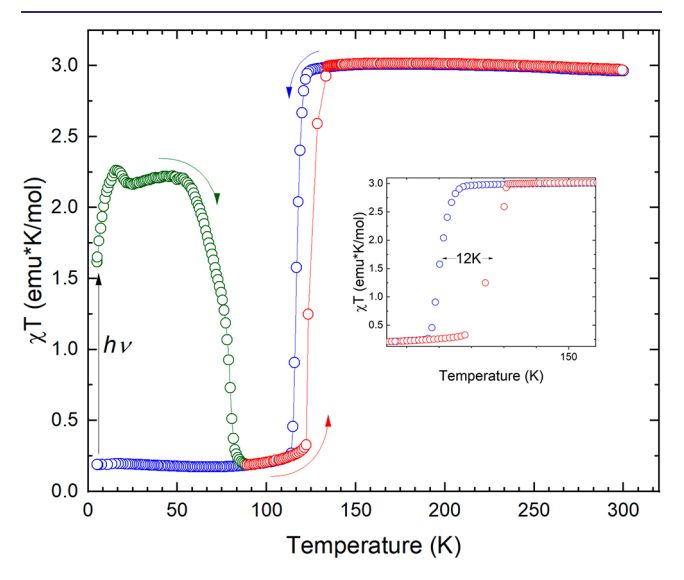


Figure 4. Temperature dependence of χT for $[Fe(tBu_2qsal)_2]$ measured while cooling (blue) and then heating (red) under applied magnetic field of 1000 Oe. The inset shows an enlarged part of the temperature range where the hysteretic spin transition takes place. The green curve corresponds to the measurement, aquired while warming, of the light-induced HS state obtained by irradiating the LS state at 5 K (as indicated with the black vertical arrow at that temperature).

LS \rightarrow HS transition occurs abruptly at $T_{1/2,\uparrow}$ = 129 K (the red curve in Figure 4), thus revealing the same 12 K wide hysteresis loop that was observed in the powder XRD data (Figure 3). The abruptness of the spin transition is well-known to depend on the strength of elastic interactions between the SCO centers. $^{41-43}$ Such interactions tend to "delay" the HS \rightarrow LS conversion upon cooling and the LS \rightarrow HS conversion upon warming, thus resulting in the opening of a hysteresis loop. The corresponding transitions in the cooling and the warming branches occur abruptly, over a few-degree temperature range, once the sufficient number of critical nucleation sites has been achieved to initiate and propagate the avalanche-like phase transition. 44,45 Obviously, the abrupt hysteretic spin transition observed for $[Fe(tBu_2qsal)_2]$ stems from the efficient intermolecular contacts within the layer of SCO molecules. Such behavior is reminiscent of another well-studied class of SCO materials based on homoleptic Fe^{II} complexes of bis(pyrazolyl)pyridine ligands,46 where efficient layered packing of SCO complexes typically leads to abrupt and hysteretic spin transitions.

Given that complexes with abrupt spin transitions frequently exhibit a light-induced excited spin state trapping (LIESST)

effect, we examined photomagnetic response of [Fe-(tBu₂qsal)₂ by irradiating the sample at 5 K within the magnetometer cavity using a fiber-optic sample holder connected to a white-light source. Irradiation led to increase in the value of magnetic moment (Figure S5), indicating the occurrence of the LIESST effect due to the light-induced excitation from the singlet LS ground state to the singlet ligand-field and MLCT states, followed by intersystem crossing to the quintet metastable HS state that becomes trapped at low temperatures.⁴⁷ The magnetic moment was monitored as a function of time, and once the increase slowed down substantially, the irradiation was stopped. The LIESST state remained stable when the temperature was maintained at 5 K (Figure S5). As the temperature was increased at a rate of 0.3 K/min, the χT increased to a plateau of ~ 2.35 emu·mol⁻¹·K (the green curve in Figure 4). This increase is associated with zero-field splitting effects typical for the HS Fe^{II} ion with S = 2. By comparing the χT value observed in the plateau region to the χT value of the HS state observed above 150 K, and subtracting the residual γT value measured in the LS state, we estimate that the light-induced LS → HS conversion proceed to \sim 77%. The incomplete conversion might be explained by the strong optical absorption of the material—a dark-green crystalline powder—that could cause insufficient penetration depth, thus preventing irradiation of the entire sample.⁴⁷ Upon heating above 60 K, the χT value decreased rapidly due to the relaxation from the metastable HS state to the ground LS state. The relaxation temperature, defined by the fastest loss of the HS state (i.e., the minimum of $d(\chi T)/dT$), was determined to be T_{LIESST} = 84 K. While these preliminary observations are promising, the LIESST behavior of [Fe(tBu₂qsal)₂] needs to be investigated in more detail, including studies of temperature- and irradiation-dependent relaxation kinetics. The results of such studies will be reported in due course.

Electronic Structure. DFT calculations were performed to examine the electronic structure of the $[Fe(tBu_2qsal)_2]$ complex in the LS and HS states. The HOMO–LUMO gap of the two spin states is 1.70 and 1.37 eV, respectively. Projected density of states (PDOS) on Fe atom for the LS complex (Figure 5a) indicates that the Fe d_{xz} , d_{yz} , and d_{xy} orbitals (the t_2 orbitals) are filled while the $d_x^2-y^2$ and d_z^2 orbitals (the e orbitals) are empty, as expected for the singlet state of the $3d^6$ transition metal ion in quasi-octahedral coordination environment. On the other hand, in the quintet HS state the electrons occupy both the t_2 and e levels (Figure

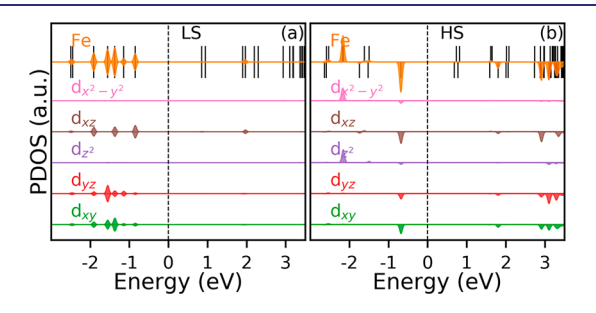


Figure 5. Electronic structure of the (a) LS and (b) HS states of the $[Fe(tBu_2qsal)_2]$ complex. Filled plots show orbital and site projections (PDOS) for the Fe atom. Horizontal lines separate spin-up and spin-down contributions to the PDOS. Vertical bars indicate energy levels of molecular orbitals. The zero-energy level is set as the middle point between HOMO and LUMO.

5b). Thus, the calculated PDOS plots are in agreement with the conventional picture of the occupation of Fe(II) ion dorbitals in SCO complexes.

Changes in the unit cell parameters calculated for the optimized crystal structure of [Fe(tBu2qsal)2] in the LS and HS states (Table S1) agree with the changes observed by the single-crystal and powder XRD (Table S1 and Figure 3, respectively). Calculations also show that the dielectric tensor for the LS and HS crystals is dominated by electronic contributions (ε_{∞}) rather than by ionic ones (ε_0) . For example, for the LS crystal the xx component of ε_{∞} is 3.249 while that of ε_0 is 0.151. Similar differences are observed for the yy and zz components of ε_{∞} and ε_{0} (Table S2). Nevertheless, an opposite situation is observed for changes in the values of ε_{∞} and ε_0 between the HS and LS states. Upon SCO, the main contribution to the difference in the corresponding diagonal components (xx, yy, zz) of the tensor arises from changes in the ionic part of the dielectric tensor (34.0%, 8.4%, and 68.5%, respectively), while the electronic part shows much smaller changes between the LS and HS states (1.1%, 0.5%, and -2.8%, respectively). The net differences in the three diagonal components of the dielectric tensor between the LS and HS states are 2.5%, 0.9%, and 1.2%, respectively (Table S2). Next, we take advantage of these changes to monitor the temperature-driven spin transition in the thin film of $[Fe(tBu_2qsal)_2]$.

SCO Behavior in Thin Film. Thin films of $[Fe(tBu_2qsal)_2]$ were successfully prepared at a sublimation temperature of 423 K and background pressure of 10^{-8} mbar onto a Pt/Ti/SiO₂/Si(100) substrate. Powder XRD patterns of films revealed that the (100) peak dominated the diffraction from the samples (Figure S6). This observation suggests the films consist of randomly oriented grains that nevertheless preserve the structural coherence related to the pronounced plate-like shape of crystallites due to the layered structure of $[Fe-(tBu_2qsal)_2]$.

Characterization of SCO in such thin films is challenging since neither conventional magnetic measurements nor XRD methods are sensitive enough for reliably monitoring changes in the properties of the films as a function of temperature. Given the calculated difference in the dielectric tensor of the LS and HS structures of $[Fe(tBu_2gsal)_2]$ and the wellestablished correlation between the spin-state switching and changes in dielectric properties,⁴⁸ we turned to capacitance measurements, which have been shown to be sensitive to abrupt changes in the dielectric constant associated with SCO in transition metal complexes.^{49–51} Frequency-dependent capacitance measurements were made on a trilayer capacitance heterojunction structure (Figure S7) containing a 20 nm thick [Fe(tBu₂qsal)₂] film sandwiched between two conducting electrodes. Results of isothermal capacitance measurements are shown in Figure 6 for both cooling (top panel) and warming (bottom panel) regimes. Upon cooling, a pronounced decrease in capacitance is observed between the 125 and 120 K isotherms. This feature extends over the entire frequency range and agrees very well with the HS \rightarrow LS transition temperature of 117 K observed in the magnetic and powder XRD measurements. Furthermore, the relative change in the capacitance observed at the spin transition is comparable to the changes in the dielectric tensor calculated for the LS and HS crystal structures (Table S2). On warming, the LS \rightarrow HS transition extends over a more restricted capacitance range

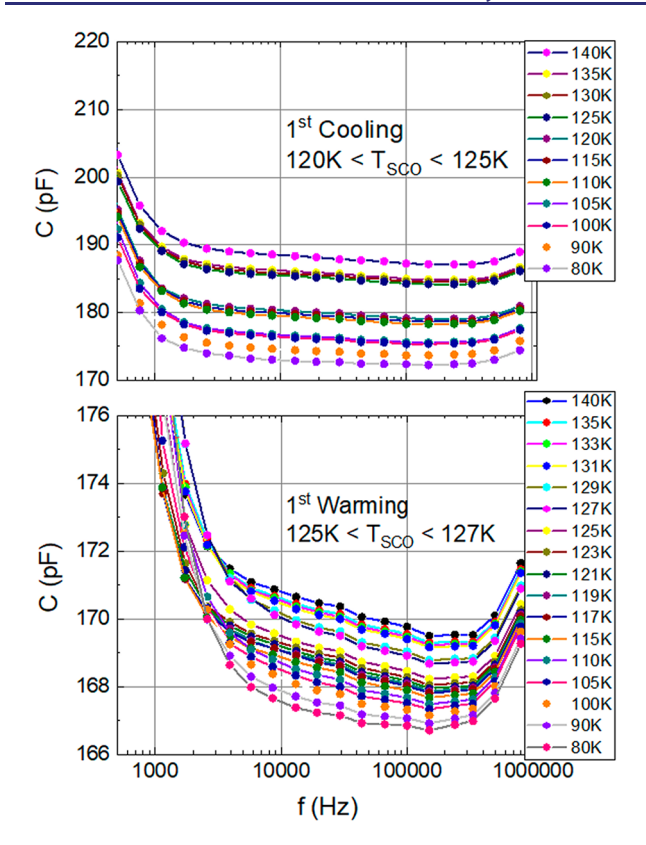


Figure 6. Frequency-dependent capacitance isotherms taken at the indicated temperatures on cooling from 300 to 50 K (top panel) and warming from 80 to 160 K (bottom panel). The abrupt SCO transition for both cooling and warming regimes is marked by a noticeable gap that extends over the entire frequency range.

spanning the 125 and 127 K isotherms. Thus, we conclude that a hysteretic spin transition is preserved in the 20 nm thick film.

The ~5 K hysteresis observed in the capacitance measurements on the thin film (Figure S8) is about 2 times smaller than the 12 K hysteresis observed in the measurements on the bulk sample (Figures 3 and 4). A similar difference in hysteresis widths was also reported in magnetization measurements of bulk and film samples of another SCO complex, Fe((Me₂Pyrz)₃BH)₂. There is however, significantly more hysteresis in the cooling/warming values of the capacitance; although the isotherms of both panels of Figure 6 cover the same temperature range, the isotherms collected on warming reflect significantly lower capacitance values. The shapes of the isothermal curves for cooling/warming are also considerably different. We make an analogy here with the typical hysteresis seen in the major/minor loops of magnetization measurements that reflect history-dependent spin distributions. On the other hand, dielectric measurements reflect history-dependent charge redistributions. Accordingly, as the Fe-N and Fe-O bond lengths increase (decrease) with increasing (decreasing) temperature (Table 1), the corresponding increases (decreases) in polarization are reflected in the capacitance changes associated with the LS \rightarrow HS (HS \rightarrow LS) transition. The spin transition is a complex conflation of all these effects, with the elongated bonds of the HS state reflecting increased polarization and hence capacitance, in agreement with the data of Figure 6.

CONCLUDING REMARKS

Two principal outcomes of this work are (1) the demonstration of a rather simple principle for the design of sublimable SCO molecules that, nevertheless, preserve strongly cooperative (and hysteretic) spin transitions in the solid state and (2) the use of a thin-film capacitor as an effective device to detect spin-state switching in ultrathin molecule-based materials. Importantly, the asymmetric design of the ligand not only provides for the different nature of intermolecular interactions on the two sides of the Fe^{II} complex but also reduces the dimensionality of these interactions, thus promoting the formation of the layered crystal structure. The study of thin films of $[Fe(tBu_2qsal)_2]$ by XRD and capacitance measurements strongly suggests that the layered character of molecular packing is preserved, at least on a short-range scale, upon deposition of the SCO material on the inorganic substrate. Such structural coherence is crucial for the preservation of the hysteretic SCO behavior that was observed in the bulk material.

We expect that our work will stimulate further studies of approaches to the design of spin-state switching materials as well as other stimuli-responsive molecule-based materials that can be utilized in 2D devices. The possibility to reduce the size of such materials by exfoliation to well-ordered molecular layers is especially intriguing, given the presence of the distinct planes of weak van der Waals interactions in their crystal structures. These studies are currently pursued in our laboratories, and their results will be reported in due course.

MATERIALS AND METHODS

Starting Materials. Iron(II) perchlorate hexahydrate (98%), triethylamine (99%), formic acid (98%), and anhydrous methanol (MeOH, HPLC grade) were obtained from Millipore Sigma; 8-aminoquinoline (>97%) was from Matrix Scientific; 3,5-di-tert-butylsalicylaldehyde (>98%) was from TCI, and anhydrous acetone (Me₂CO) was from Acros Organics. All reagents were used as received. Anhydrous acetonitrile (MeCN) was obtained by passing HPLC grade solvent (Millipore Sigma) through a system of double-drying columns packed with activated alumina and molecular sieves (Glass Contour Inc.). Elemental analysis was performed by Atlantic Microlab, Inc. (Norcross, GA).

2,4-Di(*tert***-butyl)-6-((quinoline-8-ylimino)methyl)phenol** (tBu_2qsalH). 8-Aminoquinoline (0.72 g, 5 mmol) and 3,5-di-*tert*-butylsalicylaldehyde (1.17 g, 5 mmol) were placed in a round-bottom flask. 29.5 mL of MeOH and 3 drops of formic acid were added, and the solution was stirred for 1 h under reflux. The orange solid that precipitated was isolated by filtration, washed with MeOH, and dried by suction. Yield = 0.82 g (45.6%).

[Fe(tBu₂qsal)₂] (1). Fe(ClO₄)₂·6H₂O (272 mg, 0.75 mmol) was dissolved in 15 mL of MeCN in a Schlenk tube. The ligands tBu₂qsalH (540 mg, 1.50 mmol) and Et_3N (209.1 μ L, 1.50 mmol) were dissolved in 10 mL of Me₂CO. The solution of the Fe^{II} solution was poured via cannula into the ligand solution without stirring, and the mixture was left undisturbed. Plate-shaped dark-green crystals that formed after 1 day were recovered by filtration, washed with acetone, and dried by suction. Yield = 452 mg (77.8%). Elemental analysis: calcd (found) for FeO₂N₄C₄₈H₅₄, %: C 74.41 (74.37), H 7.02 (6.98), N 7.23 (7.31).

Thermogravimetric Analysis (TGA). TGA was performed on a TGA-550 thermogravimetric analyzer (TA Instruments) in the temperature range from 300 to 700 K, at a heating rate of 10 K/min.

X-ray Diffraction (XRD). Single-crystal XRD was performed on a Rigaku-Oxford Diffraction Synergy-S diffractometer equipped with a HyPix detector and a monochromated Mo $K\alpha$ radiation source (λ = 0.71073 Å). A chosen single crystal of 1 was suspended in Parabar oil (Hampton Research) and mounted on a cryoloop, which was cooled

to the desired temperature in an $\rm N_2$ cold stream. The data set was recorded as ω -scans at 0.5° step width and integrated with the CrysAlis software package, which was also used for space group determination. 53 Empirical adsorption correction was applied based on spherical harmonics as implemented in the SCALE3 ABSPACK algorithm. 54 The crystal structure solution and refinement were performed with SHELX 55 using the interface provided by Olex2. 56 The final refinement was performed with anisotropic atomic displacement parameters for all non-hydrogen atoms. All H atoms were placed in calculated positions and refined in the riding model. Full details of the crystal structure refinement and the final structural parameters have been deposited with the Cambridge Crystallographic Data Centre (CCDC). The CCDC registry numbers and a summary of data collection and refinement are provided in Table 1.

The Rigaku Synergy-S diffractometer was also used to perform variable-temperature powder XRD by a microdiffraction method. A small amount of a powder sample of $[{\rm Fe}(t{\rm Bu_2qsal})_2]$ was mixed with Parabar oil and scooped into a cryoloop that was mounted on the goniometer head of the diffractometer and cooled to the desired temperature in an N_2 cold stream. The powder patterns were acquired at fixed temperature values between 300 and 100 K, with smaller temperature steps taken across the region corresponding to the hysteretic spin transition. The diffraction data recorded by the 2D HyPix detector were converted to 1D diffraction patterns (Figure S4) with the CrysAlis software. The unit cell refinements were performed with HighScore.

The XRD data on thin films of $[Fe(tBu_2qsal)_2]$ were recorded on a Bruker D8 Venture diffractometer at the center for X-ray crystallography in the Department of Chemistry, University of Florida. The copper X-ray source was used (λ = 1.54184 Å), and the sample-to-detector distance was adjusted to 150 mm. The 2D image shown in Figure S6 was taken as the incident angle was swept from 3.1° to 4.1°, with the exposure time of 120 s. The data were integrated and converted to a 1D diffraction pattern by using the Bruker APEX software.

Magnetic Measurements. Magnetic measurements were performed on a polycrystalline sample of [Fe(tBu₂qsal)₂] by using a Magnetic Property Measurement System (MPMS-XL, Quantum Design) equipped with a superconducting quantum interference device (SQUID) magnetometer. Direct-current (DC) magnetic susceptibility was measured in an applied magnetic field of 1000 Oe in the 1.8–350 K temperature range, with the temperature sweep rate of 1 K/min. Changing the sweep rate to 2 or 0.5 K/min did not have a pronounced effect on the hysteresis width.

Photomagnetic Measurements. Photomagnetic measurements were performed on the MPMS-XL system by using a homemade fiberoptic sample holder described elsewhere. So A Quartzline tungsten halogen lamp (400-2200 nm) delivering nominally ~ 20 mW/cm² to the sample provided the broadband "white" light. The sample was cooled to 5 K, at which point it was irradiated for the desired time in an applied magnetic field of 1000 Oe. The increase in the magnetic signal from the sample was monitored to evaluate the completeness of the LS \rightarrow HS photoconversion (Figure S5). Once the signal reached saturation, the irradiation was discontinued, and the DC magnetic susceptibility was measured as the sample was heated to 300 K at a rate of 0.3–0.5 K/min.

Thin Film Preparation. The 20 nm thick films of $[Fe(tBu_2qsal)_2]$ were deposited on $Pt/Ti/SiO_2/Si(100)$ substrates that were prepared by sequentially sputtering amorphous films of Ti (20 nm) and Pt (100 nm) onto commercial $SiO_2/Si(100)$ wavers. The films of the SCO material were deposited at a thermally regulated sublimation temperature of 423 K by using physical vapor deposition at a base pressure of 1×10^{-8} mbar and a controlled growth rate of 0.1 Å/min. The film thickness was monitored by a quartz crystal thickness monitor, and the film morphology was characterized by atomic force microscopy (AFM), finding a root-mean-square roughness of 3 nm.

Capacitance Measurements. SCO capacitors were prepared by sandwiching the 20 nm $[Fe(tBu_2qsal)_2]$ films between the top eutectic GaIn (EGaIn) electrode and the bottom $Pt/Ti/SiO_2/Si(100)$ electrode. The contact area was around 500 μ m in diameter. The

capacitance was measured by a Hewlett-Packard 4284A LCR meter with the SCO capacitor placed in a Physical Property Measurement System (PPMS, Quantum Design) under He flow. The frequency dependences of complex capacitance were measured at specific isotherms during the cooling and warming sequences. The frequency sweeps from 20 Hz to 1 MHz were made with scaling factors of 1.25 or 1.5 between successive frequencies. The temperature sweep rate before equilibrating at a given isotherm was chosen to be 1 K/min.

Quantum-Mechanical Calculations. Density functional theory calculations are performed by using the Vienna ab initio Simulation Package (VASP),⁵⁹ employing the projector-augmented wave (PAW)^{60,61} and plane-wave basis set. The generalized-gradient approximation (GGA) was used in the form of the Perdew-Burke-Ernzerhof (PBE)⁶² functional together with the DFT-D3 correction⁶³ to describe electronic exchange correlation. The electron kinetic energy cutoff for plane-wave expansion was set to 500 eV. The Brillouin zone was sampled with one point at the zone center by using a Gaussian smearing with $\sigma = 0.1$ eV for structural relaxation. All electronic cycles converged to 10^{-6} eV. The crystal structures of both HS and LS states were relaxed to minimize the stress until all components of forces acting on each atom were less than 10^{-2} eV/Å. The DFT+U method with U = 1.7 eV was used to properly describe the difference in energy between the LS and HS states of the molecular crystal (see the Supporting Information). The electronic structure of a single molecule was calculated with the Heyd-Scuseria-Ernzerhof (HSE06) hybrid functional⁶⁴ using a Gaussian smearing with σ = 50 meV. Details of the dielectric tensor calculations are provided in the Supporting Information.

ASSOCIATED CONTENT

Supporting Information

The Supporting Information is available free of charge at https://pubs.acs.org/doi/10.1021/jacs.1c04598.

Full-pattern profile fitting of powder XRD data, heat capacity, additional magnetic plots, benchmarking Hubbard *U* parameter, calculated crystal structure parameters and dielectric constants (PDF)

Accession Codes

CCDC 2080250–2080251 contain the supplementary crystallographic data for this paper. These data can be obtained free of charge via www.ccdc.cam.ac.uk/data_request/cif, or by emailing data_request/cif, or by contacting The Cambridge Crystallographic Data Centre, 12 Union Road, Cambridge CB2 1EZ, UK; fax: +44 1223 336033.

AUTHOR INFORMATION

Corresponding Author

Michael Shatruk — Department of Chemistry and Biochemistry, Florida State University, Tallahassee, Florida 32306, United States; National High Magnetic Field Laboratory, Tallahassee, Florida 32310, United States; orcid.org/0000-0002-2883-4694; Email: shatruk@chem.fsu.edu

Authors

Miguel Gakiya-Teruya — Department of Chemistry and Biochemistry, Florida State University, Tallahassee, Florida 32306, United States

Xuanyuan Jiang — Department of Physics, University of Florida, Gainesville, Florida 32611, United States

Duy Le — Department of Physics, University of Central Florida, Orlando, Florida 32816, United States;

orcid.org/0000-0001-6391-8757

- Ökten Üngör Department of Chemistry and Biochemistry, Florida State University, Tallahassee, Florida 32306, United States
- Abdullah J. Durrani Department of Physics, University of Florida, Gainesville, Florida 32611, United States
- John J. Koptur-Palenchar Department of Physics, University of Florida, Gainesville, Florida 32611, United States
- Jun Jiang Department of Physics, University of Florida, Gainesville, Florida 32611, United States
- Tao Jiang Department of Physics, University of Central Florida, Orlando, Florida 32816, United States
- Mark W. Meisel Department of Physics and National High Magnetic Field Laboratory, University of Florida, Gainesville, Florida 32611, United States; orcid.org/0000-0003-4980-5427
- Hai-Ping Cheng Department of Physics, University of Florida, Gainesville, Florida 32611, United States
- Xiao-Guang Zhang Department of Physics, University of Florida, Gainesville, Florida 32611, United States;
 orcid.org/0000-0003-0092-5006
- Xiao-Xiao Zhang Department of Physics, University of Florida, Gainesville, Florida 32611, United States;
 o orcid.org/0000-0002-5447-3394
- Talat S. Rahman Department of Physics, University of Central Florida, Orlando, Florida 32816, United States; orcid.org/0000-0003-3889-7776
- Arthur F. Hebard Department of Physics, University of Florida, Gainesville, Florida 32611, United States

Complete contact information is available at: https://pubs.acs.org/10.1021/jacs.1c04598

Notes

The authors declare no competing financial interest.

ACKNOWLEDGMENTS

This work was supported as part of the Center for Molecular Magnetic Quantum Materials, an Energy Frontier Research Center funded by the U.S. Department of Energy, Office of Science, Basic Energy Sciences, under Award DESC0019330. The work was also supported, in part, by the National Science Foundation (NSF) via Awards DMR-1708410 (M.W.M.) and DMR-1644779 (National High Magnetic Field Laboratory). The Rigaku Synergy-S single-crystal X-ray diffractometer used for crystallographic work was acquired through the NSF MRI program (Award CHE-1828362). Computational resources were provided by the National Energy Research Scientific Computing Center (NERSC). This research also used resources provided by the X-ray Crystallography Center (FSU075000XRAY) and the Materials Characterization Laboratory (FSU075000MAC) at the FSU Department of Chemistry and Biochemistry.

ABBREVIATIONS

2D, two-dimensional; CCDC, Cambridge Crystallographic Data Centre; DFT, density functional theory; HS, high spin; LIESST, light-induced excited spin state trapping; LS, low spin; PDOS, projected density of states; SCO, spin crossover; XRD, X-ray diffraction.

REFERENCES

(1) Gütlich, P.; Goodwin, H. A. Spin crossover - an overall perspective. *Top. Curr. Chem.* **2004**, 233, 1–47.

- (2) Jakobsen, V. B.; Trzop, E.; Gavin, L. C.; Dobbelaar, E.; Chikara, S.; Ding, X.; Esien, K.; Müller-Bunz, H.; Felton, S.; Zapf, V. S.; Collet, E.; Carpenter, M. A.; Morgan, G. G. Stress-induced domain wall motion in a ferroelastic Mn³⁺ spin crossover complex. *Angew. Chem., Int. Ed.* **2020**, *59*, 13305–13312.
- (3) Murphy, M. J.; Zenere, K. A.; Ragon, F.; Southon, P. D.; Kepert, C. J.; Neville, S. M. Guest programmable multistep spin crossover in a porous 2-D Hofmann-type material. *J. Am. Chem. Soc.* **2017**, *139*, 1330–1335.
- (4) Lemke, H. T.; Kjær, K. S.; Hartsock, R.; van Driel, T. B.; Chollet, M.; Glownia, J. M.; Song, S.; Zhu, D.; Pace, E.; Matar, S. F.; Nielsen, M. M.; Benfatto, M.; Gaffney, K. J.; Collet, E.; Cammarata, M. Coherent structural trapping through wave packet dispersion during photoinduced spin state switching. *Nat. Commun.* **2017**, *8*, 15342.
- (5) Zerdane, S.; Wilbraham, L.; Cammarata, M.; Iasco, O.; Rivière, E.; Boillot, M. L.; Ciofini, I.; Collet, E. Comparison of structural dynamics and coherence of d–d and MLCT light-induced spin state trapping. *Chem. Sci.* **2017**, *8*, 4978–4986.
- (6) Auböck, G.; Chergui, M. Sub-50-fs photoinduced spin crossover in [Fe(bpy)₃]²⁺. *Nat. Chem.* **2015**, *7*, 629–633.
- (7) Marino, A.; Chakraborty, P.; Servol, M.; Lorenc, M.; Collet, E.; Hauser, A. The role of ligand-field states in the ultrafast photophysical cycle of the prototypical iron(II) spin-crossover compound [Fe-(ptz)₆](BF₄)₂. Angew. Chem., Int. Ed. **2014**, 53, 3863–3867.
- (8) Ye, S. F.; Neese, F. Accurate modeling of spin-state energetics in spin-crossover systems with modern density functional theory. *Inorg. Chem.* **2010**, *49*, 772–774.
- (9) Cirera, J.; Ruiz, E. Computational modeling of transition temperatures in spin-crossover systems. *Comments Inorg. Chem.* **2019**, 39, 216–241.
- (10) Cirera, J.; Via-Nadal, M.; Ruiz, E. Benchmarking density functional methods for calculation of state energies of first row spin-crossover molecules. *Inorg. Chem.* **2018**, *57*, 14097–14105.
- (11) Pham, C. H.; Cirera, J.; Paesani, F. Molecular mechanisms of spin crossover in the {Fe(pz)[Pt(CN)₄]} metal—organic framework upon water adsorption. *J. Am. Chem. Soc.* **2016**, *138*, 6123–6126.
- (12) Harzmann, G. D.; Frisenda, R.; van der Zant, H. S. J.; Mayor, M. Single-molecule spin switch based on voltage-triggered distortion of the coordination sphere. *Angew. Chem., Int. Ed.* **2015**, *54*, 13425–13430
- (13) Koo, Y. S.; Galan-Mascaros, J. R. Spin crossover probes confer multistability to organic conducting polymers. *Adv. Mater.* **2014**, *26*, 6785–6789.
- (14) Chikara, S.; Gu, J.; Zhang, X. G.; Cheng, H.-P.; Smythe, N.; Singleton, J.; Scott, B.; Krenkel, E.; Eckert, J.; Zapf, V. S. Magnetoelectric behavior via a spin state transition. *Nat. Commun.* **2019**, *10*, 4043.
- (15) Phan, H.; Benjamin, S. M.; Steven, E.; Brooks, J. S.; Shatruk, M. Photomagnetic response in highly conductive iron(II) spin-crossover complexes with TCNQ radicals. *Angew. Chem., Int. Ed.* **2015**, *54*, 823–827.
- (16) Bairagi, K.; Iasco, O.; Bellec, A.; Kartsev, A.; Li, D.; Lagoute, J.; Chacon, C.; Girard, Y.; Rousset, S.; Miserque, F.; Dappe, Y. J.; Smogunov, A.; Barreteau, C.; Boillot, M.-L.; Mallah, T.; Repain, V. Molecular-scale dynamics of light-induced spin cross-over in a two-dimensional layer. *Nat. Commun.* **2016**, *7*, 12212.
- (17) Dugay, J.; Aarts, M.; Giménez-Marqués, M.; Kozlova, T.; Zandbergen, H. W.; Coronado, E.; van der Zant, H. S. J. Phase transitions in spin-crossover thin films probed by graphene transport measurements. *Nano Lett.* **2017**, *17*, 186–193.
- (18) Burzurí, E.; García-Fuente, A.; García-Suárez, V.; Senthil Kumar, K.; Ruben, M.; Ferrer, J.; van der Zant, H. S. J. Spin-state dependent conductance switching in single molecule-graphene junctions. *Nanoscale* **2018**, *10*, 7905–7911.
- (19) Ridier, K.; Bas, A.-C.; Zhang, Y.; Routaboul, L.; Salmon, L.; Molnár, G.; Bergaud, C.; Bousseksou, A. Unprecedented switching endurance affords for high-resolution surface temperature mapping using a spin-crossover film. *Nat. Commun.* **2020**, *11*, 3611.

- (20) Miyamachi, T.; Gruber, M.; Davesne, V.; Bowen, M.; Boukari, S.; Joly, L.; Scheurer, F.; Rogez, G.; Yamada, T. K.; Ohresser, P.; Beaurepaire, E.; Wulfhekel, W. Robust spin crossover and memristance across a single molecule. *Nat. Commun.* **2012**, *3*, 938.
- (21) Gopakumar, T. G.; Bernien, M.; Naggert, H.; Matino, F.; Hermanns, C. F.; Bannwarth, A.; Mühlenberend, S.; Krüger, A.; Krüger, D.; Nickel, F.; Walter, W.; Berndt, R.; Kuch, W.; Tuczek, F. Spin-crossover complex on Au(111): structural and electronic differences between mono- and multilayers. *Chem. Eur. J.* **2013**, *19*, 15702–15709.
- (22) Ossinger, S.; Naggert, H.; Kipgen, L.; Jasper-Toennies, T.; Rai, A.; Rudnik, J.; Nickel, F.; Arruda, L. M.; Bernien, M.; Kuch, W.; Berndt, R.; Tuczek, F. Vacuum-evaporable spin-crossover complexes in direct contact with a solid surface: bismuth versus gold. *J. Phys. Chem. C* 2017, 121, 1210–1219.
- (23) Gruber, M.; Berndt, R. Spin-crossover complexes in direct contact with surfaces. *Magnetochemistry* **2020**, *6*, 35.
- (24) Kumar, K. S.; Ruben, M. Sublimable spin-crossover complexes: from spin-state switching to molecular devices. *Angew. Chem., Int. Ed.* **2021**, *60*, 7502–7521.
- (25) Han, H.; Zhou, Z.; Carozza, J. C.; Lengyel, J.; Yao, Y.; Wei, Z.; Dikarev, E. V. From lithium to sodium: design of heterometallic molecular precursors for the $NaMO_2$ cathode materials. *Chem. Commun.* **2019**, *55*, 7243–7246.
- (26) Pasko, S.; Hubert-Pfalzgraf, L. G.; Abrutis, A. Synthesis and characterization of hafnium tert-butylacetoacetate as new MOCVD precursor for HfO₂ films. *Mater. Lett.* **2005**, *59*, 1836–1840.
- (27) Derraz, Y.; Cyr-Athis, O.; Choukroun, R.; Valade, L.; Cassoux, P.; Dahan, F.; Teyssandier, F. tert-Butyl-substituted vanadocene, (C₅H₄CMe₃)₂V: a precursor for MOCVD of pure vanadium carbide. *J. Mater. Chem.* **1995**, *5*, 1775–1778.
- (28) Weber, B.; Kaps, E. S.; Obel, J.; Achterhold, K.; Parak, F. G. Synthesis and characterization of a dinuclear iron(II) spin crossover complex with wide hysteresis. *Inorg. Chem.* **2008**, *47*, 10779–10787.
- (29) Lochenie, C.; Heinz, J.; Milius, W.; Weber, B. Iron(II) spin crossover complexes with diaminonaphthalene-based Schiff base-like ligands: mononuclear complexes. *Dalton Trans.* **2015**, 44, 18065—18077.
- (30) Schönfeld, S.; Lochenie, C.; Thoma, P.; Weber, B. 1D iron(II) spin crossover coordination polymers with 3,3'-azopyridine kinetic trapping effects and spin transition above room temperature. *CrystEngComm* **2015**, *17*, 5389–5395.
- (31) Handel, R. W.; Willms, H.; Jameson, G. B.; Berry, K. J.; Moubaraki, B.; Murray, K. S.; Brooker, S. Factors influencing the structural and magnetic properties of octahedral cobalt(II) and iron(II) complexes of terdentate N₃ Schiff base ligands. *Eur. J. Inorg. Chem.* **2010**, 2010, 3317–3327.
- (32) Kulmaczewski, R.; Cespedes, O.; Halcrow, M. A. Gradual thermal spin-crossover mediated by a reentrant $Z'=\vec{1}$ $Z'=\vec{6}$ Z'=1 phase transition. *Inorg. Chem.* **2017**, *56*, 3144–3148.
- (33) Senthil Kumar, K.; Bayeh, Y.; Gebretsadik, T.; Elemo, F.; Gebrezgiabher, M.; Thomas, M.; Ruben, M. Spin-crossover in iron(ii)-Schiff base complexes. *Dalton Trans.* **2019**, *48*, 15321–15337.
- (34) Kurz, H.; Hörner, G.; Weber, B. An iron(II) spin crossover complex with a maleonitrile Schiff base-like ligand and scan rate-dependent hysteresis above room temperature. *Z. Anorg. Allg. Chem.* **2021**, *647*, 896–904.
- (35) Schönfeld, S.; Bauer, W.; Thallmair, S.; Hörner, G.; Weber, B. Running in the family: molecular factors controlling spin crossover of iron(II) complexes with Schiff-base like ligands. *Z. Anorg. Allg. Chem.* **2021**, *647*, 905–914.
- (36) Gong, D.; Wang, B.; Jia, X.; Zhang, X. The enhanced catalytic performance of cobalt catalysts towards butadiene polymerization by introducing a labile donor in a salen ligand. *Dalton Trans.* **2014**, 43, 4169–4178.
- (37) Rotthaus, O.; Labet, V.; Philouze, C.; Jarjayes, O.; Thomas, F. Pseudo-octahedral Schiff base nickel(II) complexes: does single oxidation always lead to the nickel(III) valence tautomer? *Eur. J. Inorg. Chem.* **2008**, 2008, 4215–4224.

- (38) Guionneau, P.; Marchivie, M.; Bravic, G.; Létard, J. F.; Chasseau, D. Structural aspects of spin crossover. Example of the $[Fe^{II}L_n(NCS)_2]$ complexes. *Top. Curr. Chem.* **2004**, 234, 97–128.
- (39) Kuroda-Sowa, T.; Yu, Z.; Senzaki, Y.; Sugimoto, K.; Maekawa, M.; Munakata, M.; Hayami, S.; Maeda, Y. Abrupt spin transitions and LIESST effects observed in Fe^{II} spin-crossover complexes with extended π -conjugated Schiff-base ligands having N₄O₂ donor sets. *Chem. Lett.* **2008**, *37*, 1216–1217.
- (40) Atzori, M.; Poggini, L.; Squillantini, L.; Cortigiani, B.; Gonidec, M.; Bencok, P.; Sessoli, R.; Mannini, M. Thermal and light-induced spin transition in a nanometric film of a new high-vacuum processable spin crossover complex. *J. Mater. Chem. C* **2018**, *6*, 8885–8889.
- (41) Chakraborty, P.; Enachescu, C.; Walder, C.; Bronisz, R.; Hauser, A. Thermal and light-induced spin switching dynamics in the 2D coordination network of $\{[Zn_{1-x}Fe_x(bbtr)_3](ClO_4)_2\}_{\infty}$: the role of cooperative effects. *Inorg. Chem.* **2012**, *51*, 9714–9722.
- (42) Halcrow, M. A. Structure:function relationships in molecular spin-crossover complexes. *Chem. Soc. Rev.* **2011**, *40*, 4119–4142.
- (43) Palii, A.; Ostrovsky, S.; Reu, O.; Tsukerblat, B.; Decurtins, S.; Liu, S.-X.; Klokishner, S. Microscopic theory of cooperative spin crossover: Interaction of molecular modes with phonons. *J. Chem. Phys.* **2015**, *143*, No. 084502.
- (44) Enachescu, C.; Hauser, A. Study of switching in spin transition compounds within the mechanoelastic model with realistic parameters. *Phys. Chem. Chem. Phys.* **2016**, *18*, 20591–20599.
- (45) Slimani, A.; Varret, F.; Boukheddaden, K.; Garrot, D.; Oubouchou, H.; Kaizaki, S. Velocity of the high-spin low-spin interface inside the thermal hysteresis loop of a spin-crossover crystal, via photothermal control of the interface motion. *Phys. Rev. Lett.* **2013**, *110*, 087208.
- (46) Kershaw Cook, L. J.; Mohammed, R.; Sherborne, G.; Roberts, T. D.; Alvarez, S.; Halcrow, M. A. Spin state behavior of iron(II)/dipyrazolylpyridine complexes. New insights from crystallographic and solution measurements. *Coord. Chem. Rev.* **2015**, 289–290, 2–12.
- (47) Hauser, A. Light-induced spin crossover and the high-spin low-spin relaxation. *Top. Curr. Chem.* **2004**, 234, 155–198.
- (48) Lefter, C.; Davesne, V.; Salmon, L.; Molnár, G.; Demont, P.; Rotaru, A.; Bousseksou, A. Charge transport and electrical properties of spin crossover materials: towards nanoelectronic and spintronic devices. *Magnetochemistry* 2016, 2, 18.
- (49) Bousseksou, A.; Molnár, G.; Demont, P.; Menegotto, J. Observation of a thermal hysteresis loop in the dielectric constant of spin crossover complexes: towards molecular memory devices. *J. Mater. Chem.* **2003**, *13*, 2069–2071.
- (50) Bonhommeau, S.; Guillon, T.; Lawson Daku, L. M.; Demont, P.; Sanchez Costa, J.; Létard, J.-F.; Molnár, G.; Bousseksou, A. Photoswitching of the dielectric constant of the spin-crossover complex [Fe(L)(CN)₂]·H₂O. *Angew. Chem., Int. Ed.* **2006**, 45, 1625–1629.
- (51) Iazzolino, A.; Galle, G.; Degert, J.; Létard, J. F.; Freysz, E. Impact of the spin state switching on the dielectric constant of iron(II) spin crossover nanoparticles. *Chem. Phys. Lett.* **2015**, *641*, 14–19
- (52) Mallah, T.; Cavallini, M. Surfaces, thin films and patterning of spin crossover compounds. C. R. Chim. 2018, 21, 1270–1286.
- (53) CrysAlis; Oxford Diffraction Ltd.: Abingdon, England, 2006.
- (54) SCALE3 ABSPACK An Oxford Diffraction program (1.0.4, gui:1.0.3); Oxford Diffraction Ltd.: Abingdon, England, 2005.
- (55) Sheldrick, G. M. Crystal structure refinement with SHELXL. Acta Crystallogr., Sect. C: Struct. Chem. 2015, 71, 3–8.
- (56) Dolomanov, O. V.; Bourhis, L. J.; Gildea, R. J.; Howard, J. A. K.; Puschmann, H. OLEX2: a complete structure solution, refinement and analysis program. *J. Appl. Crystallogr.* **2009**, *42*, 339–341.
- (57) X'Pert HighScore Plus software v. 2.2b; PANalytical B.V.: Almelo, Netherlands, 2006.
- (58) Knowles, E. S. Strain-Mediated Photomagnetic Effects in Heterostructured Nanoparticles of Prussian Blue Analogues. Ph.D. Thesis, University of Florida, Gainesville, FL, 2013.

- (59) Kresse, G.; Furthmüller, J. Efficiency of ab-initio total energy calculations for metals and semiconductors using a plane-wave basis set. *Comput. Mater. Sci.* **1996**, *6*, 15–50.
- (60) Blöchl, P. E. Projector augmented-wave method. Phys. Rev. B: Condens. Matter Mater. Phys. 1994, 50, 17953–17979.
- (61) Kresse, G.; Joubert, D. From ultrasoft pseudopotentials to the projector augmented-wave method. *Phys. Rev. B: Condens. Matter Mater. Phys.* **1999**, *59*, 1758–1775.
- (62) Perdew, J. P.; Burke, K.; Ernzerhof, M. Generalized Gradient Approximation Made Simple. *Phys. Rev. Lett.* **1996**, *77*, 3865–3868.
- (63) Grimme, S.; Antony, J.; Ehrlich, S.; Krieg, H. A consistent and accurate ab initio parametrization of density functional dispersion correction (DFT-D) for the 94 elements H-Pu. *J. Chem. Phys.* **2010**, 132, 154104–154122.
- (64) Heyd, J.; Scuseria, G. E.; Ernzerhof, M. Hybrid functionals based on a screened Coulomb potential. *J. Chem. Phys.* **2003**, *118*, 8207–8215.